Received: 19 March 2019 | Revised: 21 June 2019 | Accepted: 4 July 2019

DOI: 10.1111/jace.16693



Journal of the American Ceramic Society

ORIGINAL ARTICLE

# On comparison of luminescence properties of $La_2Zr_2O_7$ and $La_2Hf_2O_7$ nanoparticles

**Santosh K. Gupta**[1,2] | **Maya Abdou**[1] | **Partha S. Ghosh**[3] | **Jose P. Zuniga**[1] | **Ezhilarasan Manoharan**[4] | **HyeongJun Kim**[4] | **Yuanbing Mao**[1,5]

[1]Department of Chemistry, University of Texas Rio Grande Valley, Edinburg, TX, USA

[2]Radiochemistry Division, Bhabha Atomic Research Centre, Mumbai, India

[3]Materials Science Division, Bhabha Atomic Research Centre, Mumbai, India

[4]Department of Physics and Astronomy, University of Texas Rio Grande Valley, Edinburg, TX, USA

[5]School of Earth, Environmental, and Marine Sciences, University of Texas Rio Grande Valley, Edinburg, TX, USA

**Correspondence**
Yuanbing Mao, Department of Chemistry, University of Texas Rio Grande Valley, 1201 West University Drive, Edinburg, TX 78539, USA.
Email: yuanbing.mao@utrgv.edu

**Funding information**
National Science Foundation under DMR, Grant/Award Number: 1523577; National Science Foundation under CHE, Grant/Award Number: 1710160

## Abstract

Unveiling the underlying mechanisms of properties of functional materials, including the luminescence differences among similar pyrochlores $A_2B_2O_7$, opens new gateways to select proper hosts for various optoelectronic applications by scientists and engineers. For example, although $La_2Zr_2O_7$ (LZO) and $La_2Hf_2O_7$ (LHO) pyrochlores have similar chemical compositional and crystallographic structural features, they demonstrate different luminescence properties both before and after doped with $Eu^{3+}$ ions. Based on our earlier work, LHO-based nanophosphors display higher photo- and radioluminescence intensity, higher quantum efficiency, and longer excited state lifetime compared to LZO-based nanophosphors. Moreover, under electronic $O^{2-} \rightarrow Zr^{4+}/Hf^{4+}$ transition excitation at 306 nm, undoped LHO nanoparticles (NPs) have only violet blue emission, whereas LZO NPs show violet blue and red emissions. In this study, we have combined experimental and density functional theory (DFT) based theoretical calculation to explain the observed results. First, we calculated the density of state (DOS) based on DFT and studied the energetics of ionized oxygen vacancies in the band gaps of LZO and LHO theoretically, which explain their underlying luminescence difference. For $Eu^{3+}$-doped NPs, we performed emission intensity and lifetime calculations and found that the LHOE NPs have higher host to dopant energy transfer efficiency than the LZOE NPs (59.3% vs 24.6%), which accounts for the optical performance superiority of the former over the latter. Moreover, by corroborating our experimental data with the DFT calculations, we suggest that the $Eu^{3+}$ doping states in LHO present at exact energy position (both in majority and minority spin components) where oxygen defect states are located unlike those in LZO. Lastly, both the NPs show negligible photobleaching highlighting their potential for bioimaging applications. This current report provides a deeper understanding of the advantages of LHO over LZO as an advanced host for phosphors, scintillators, and fluoroimmunoassays.

**KEYWORDS**

DFT, Europium, $La_2Hf_2O_7$, $La_2Zr_2O_7$, photoluminescence, radioluminescence

  

## 1 | INTRODUCTION

In the past decades, materials with $A_2B_2O_7$ composition (A is trivalent and B is tetravalent ion) have been explored extensively due to their various unique characteristics such as low thermal conductivity, high radiation stability, high dielectric constant, suitable band gap, high refractive index, along with ease of synthesis, high mechanical strength, and high thermal stability, etc. These properties make them suitable for scientific and technological applications such as thermal barrier coatings,[1] magnetic materials,[2,3] electrocatalysis,[4,5] sensors,[6] optical materials,[7] solid-oxide fuel cells,[8] high level nuclear waste hosts,[9] etc. Moreover, recently relevant nanostructured pyrochlore materials have gained significant attention compared with their bulk counterparts in the areas of photoluminescence,[10–13] scintillation,[11–13] and magnetism.[14]

In this context, $La_2Zr_2O_7$ and $La_2Hf_2O_7$ have been two standout pyrochlores for their suitability in various kinds of technological applications such as luminescence, scintillator, ferroelectric material, nuclear waste host, catalyst, and electrode material in fuel cells, etc.[9,11–13,15–20] They are thermally stable, can accommodate dopant ions at both A and B sites, and have high radiation stability, etc. Hence, they are predominately used as hosts in the production of doped inorganic phosphors.[11,21–25] Moreover, lanthanum-based pyrochlores are known to exhibit excellent thermal stability, high thermal shock resistance, and fracture toughness compared to ytrria-stabilized zirconia (YSZ).[26] For example, Hansel et al have explored the variation in luminescence lifetime of $Eu^{3+}$ ions in $La_2Zr_2O_7$ and $La_2Hf_2O_7$ hosts as a function of temperature for possible applications in non-contact thermometry.[27]

However, the literature pertaining to photoluminescence study in undoped $La_2B_2O_7$ (B = Zr and Hf) and their comparison is completely missing, though there have been reports for $Nd_2Zr_2O_7$, $Gd_2Zr_2O_7$, $Y_2Zr_2O_7$, and $Eu_2Zr_2O_7$.[28–30] Eagleman et al observed blue emission in bulk $La_2Hf_2O_7$ powder induced by oxygen vacancies but could not assign the exact types of oxygen vacancies involved.[31] Zhang et al did not observe any appreciable emission from their $La_2Zr_2O_7$ nanocrystals, but after sensitizing with a $Pb^{2+}$ ions, they observed weak emission which was attributed to the transition between valence band and oxygen vacancies (mid-gap level).[30] Moreover, the exact structure of oxygen vacancies involved in such luminescence phenomenon (neutral, singly ionized, or doubly ionized) needs to be identified for explicitly proposing exact mechanisms. In that context, density functional theory (DFT) studies stand out in deciphering the suitable model and mechanism involved in defect induced emission as reported for perovskite, pyrochlore, and spinel, etc.[28,29,32,33]

Most optical and structural investigations of $A_2B_2O_7$ pyrochlores have been focused on the effect of substitutions in the $A^{3+}$ ions, especially in cases where the substitution is not charge compensated. Much less attention has been paid to the impact by $B^{4+}$ site substitution, which could have significant effects on the structure of pyrochlore hosts that consequently affect the spectral properties. Recent studies on zirconate based phosphors show that, $Zr^{4+}$ exists in $d^0$ configuration play a very decisive role in ligand to metal charge transfer (LMCT).[34] There are only a few independent reports on the luminescence studies of $La_2X_2O_7$:$Eu^{3+}$ (X = Zr and Hf), but comparative studies for the observed differences are missing, not to mention the understanding of the underlying mechanisms both experimentally and theoretically, including the energetics of ionized oxygen vacancies, the host to dopant energy transfer, and non-radiative channels.[10–12,22,23]

Doping host materials is an efficient way to synthesize tunable luminescent phosphors. Moreover, doping can shift the light emission from undoped $La_2B_2O_7$ (B = Zr and Hf) NPs to other regions. Trivalent europium ion has been the most extensively used spectroscopic probe, and it can easily sense any change in the structure and optical properties of host materials, so we chose it for this work.[35] More specifically, to compare the optical properties of doped $La_2B_2O_7$ (B = Zr and Hf) NPs, we have doped $Eu^{3+}$ ions into these two hosts to take advantages of the degenerated $^5D_0$ and $^7F_0$ states, presence of pure magnetic dipole and hypersensitive electric dipole transitions, and very bright and narrow red band due to the $^5D_0 \rightarrow {}^7F_2$ transition.

The photophysical properties of luminescent $Eu^{3+}$ ions are strongly governed by the local environment, which depends on the crystal field surrounding the emitting ion. In our earlier work, we focused on separate exploration of the effect of $Eu^{3+}$ doping concentration, effect of molten salt processing time, effect annealing temperature, effect of co-precipitating pH on the emission output, quantum efficiency, radioluminescence output and excited state lifetime of $La_2Zr_2O_7$ and $La_2Hf_2O_7$ NPs.[11,12,36–39] Molten salt synthesis has several advantages for an unique materials synthesis method, such as low formation temperature, environment benignness, simple to operate in normal research laboratory, easy to scale up, and cost efficient.[40] From these studies, we found that the $La_2Hf_2O_7$-based NPs display better luminescence and scintillation performance compared to the $La_2Zr_2O_7$ NPs, but could not understand the underlying reasons for their luminescence differences.

In this work, we have undertaken detailed comparative analysis towards understanding the energetics of defect electronic states, position of $O^{2-} \rightarrow Eu^{3+}$ charge transfer state, photon emission, asymmetry ratio, excited state lifetime, and dynamics of host-dopant energy transfer in $La_2Zr_2O_7$ and $La_2Hf_2O_7$. Localized displacements of atoms induced by dopants, especially, the highly localized nature of the structural distortions caused by ionic charge and size mismatch between $Eu^{3+}$ dopant and $La^{3+}/Zr^{4+}/Hf^{4+}$ ions, would be supported by theoretical simulations.[28,41] Therefore, we have

taken a great effort using DFT calculations for both undoped and $Eu^{3+}$ doped $La_2Zr_2O_7$ and $La_2Hf_2O_7$ NPs in this work to support our experimental results. This work provides a fundamental understanding of the luminescence differences on the molecular level of the $La_2B_2O_7$ (B = Zr or Hf) NPs. Both experimental and DFT calculation results have confirmed that the LHOE NPs display better optical performance than the LZOE NPs in terms of quantum efficiency, excited state lifetime, and radioluminescence output which are attributed to better host to dopant energy transfer efficiency in the LHOE NPs. The high optical transparency offered by single crystals has huge advantages particularly for detection of ionizing radiations. Compared to nanoparticles (NPs), their synthesis is highly cost intensive and requires ultra-pure chemicals, highly sophisticated instrumentation, and long processing time (as long as 6 months).[42–44] Lastly, both the LZOE and LHOE NPs have shown minimal luminescence photobleaching under prolonged exposure to 532 nm laser for 10 minutes. Their superior photostabilities underscore the bioimaging feasibility of the LZOE and LHOE NPs for fluorescence-based assays. The obtained information is highly beneficial in selecting better host for designing highly efficient pyrochlore based RE based phosphors for red emitting luminescence, scintillator, and fluoroimmunoassays.

## 2 | EXPERIMENTAL

In this study, both undoped and 5% $Eu^{3+}$-doped $La_2Zr_2O_7$ and $La_2Hf_2O_7$ NPs were synthesized using a combined coprecipitation and molten salts synthesis technique (Figure S1) as reported in our earlier work.[13,22] The undoped $La_2Zr_2O_7$ and $La_2Hf_2O_7$ NPs are designated as LZO and LHO whereas the $Eu^{3+}$ doped samples are designated as LZOE and LHOE. The details on the synthesis, characterization, and theoretical methodology adopted for the LZO and LHO NPs are described as Figures S1-S3, respectively. Furthermore, the sample preparation details for fluorescence microscopy are given in Figure S4.

## 3 | RESULTS AND DISCUSSION

### 3.1 | Phase, structure, and morphology of the NPs

XRD patterns of the LZO, LHO, LZOE, and LHOE NPs (Figure 1A) confirmed that all samples are single phase and highly crystalline. No other impurity phase such as $La_2O_3$, $ZrO_2$, or $HfO_2$ is detected. Also, there is no visible change in the XRD pattern after $Eu^{3+}$ doping of both LZO and LHO NPs.

Pyrochlore is a superstructure of a fluorite-like array of atoms. Superlattice diffraction of the (331) and (511) peaks

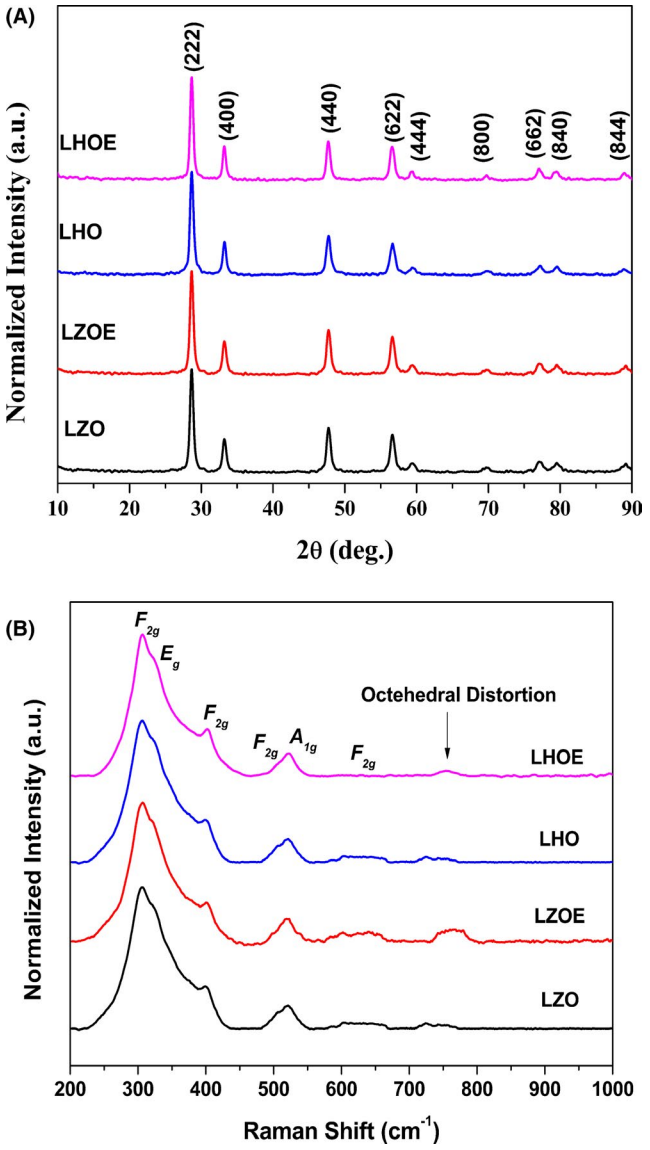


**FIGURE 1** (A) Powder XRD patterns and (B) Raman spectra of the undoped and Eu-doped $La_2Zr_2O_7$ and $La_2Hf_2O_7$ NPs [Color figure can be viewed at wileyonlinelibrary.com]

are the characteristic ones of the pyrochlore structure to be distinguished from the fluorite structure.[45] Due to proximity in structure and low power of common lab diffractometer, it is difficult to distinguish the fluorite and pyrochlore structures using XRD. Therefore, the diffraction patterns from our NPs are indexed based on the fluorite structure with F*m*-3*m* space group (JCPDS-78-1292 for $La_2Hf_2O_7$[13] and JCPDS-17-0450 for $La_2Zr_2O_7$[22]). The structure of $La_2Hf_2O_7$ with 8-coordinated lanthanum scalenohedra and 6-coordinated Hf/Zr octahedra is shown in Figure S2.

The calculated lattice parameter remained the same for LHO and LHOE but indicated a slight reduction from LZO to LZOE (Table 1). It is possible that a fraction of larger sized $Eu^{3+}$ ions residing at smaller $Hf^{4+}$ site in case of the LHOE NPs is less than that residing at $Zr^{4+}$ site in case of the

**TABLE 1** Calculated lattice parameter and crystallite size by the Bragg's equation and the Debye-Scherrer equation for undoped and Eu-doped LZO and LHO NPs

| Samples | 2θ (°) | FWHM ($\beta$) | Lattice parameters (Å) | Crystallite size (nm) |
|---|---|---|---|---|
| LZO | 28.50 | 0.456 | 10.84 | 17.4 |
| LZOE | 28.59 | 0.359 | 10.80 | 14.1 |
| LHO | 28.74 | 0.302 | 10.75 | 26.3 |
| LHOE | 28.72 | 0.382 | 10.75 | 20.7 |

LZOE NPs. The calculated crystalline size is reduced upon $Eu^{3+}$ doping in the LZO and LHO NPs. This is attributed to lattice distortion caused by radius difference between the dopant and the replaced ions in case of $Eu^{3+}$ occupying $Hf^{4+}$/$Zr^{4+}$. The distortion is caused by lattice strain which invokes the need of charge compensating defect with the formation of oxygen vacancies due to the size and charge mismatch.

Disordered fluorite phase exists in $Fm\bar{3}m$ space group wherein all the cationic ions ($A^{3+}$ and $B^{4+}$) are randomly distributed allowing for one active Raman mode. On the other hand, ordered pyrochlore phase exists in $Fd\bar{3}m$ space group. There are two cationic sites, three anionic sites as 48f ($O_x$), 8a ($O_y$), and 8b ($O_z$), and 1/8th of absent oxygen ions ($O_z$) at 8b site, so the pyrochlore structure has six active Raman modes. Therefore, Raman spectroscopy is used to determine the local structure of the synthesized NPs because of its high sensitivity to the different M-O vibrational modes (Figure 1B). Raman spectra from our NPs displayed six distinct peaks at 307, 322, 395, 493, 511, and 595 $cm^{-1}$ corresponding to $A_{1g}$, $E_g$, and $4F_{2g}$ modes which are typical of ordered pyrochlore structure.[46] Specifically, the Raman vibrations at lower frequencies around 307, 322, 395 $cm^{-1}$ due to $F_{2g}$, $E_g$, and $F_{2g}$ modes arise from vibrations of the La–O and Zr–O/Hf–O bonds whereas the higher frequencies of $F_{2g}$ modes arise from stretching of the Zr–O/Hf–O bonds. The Raman mode at 750 $cm^{-1}$ in both hosts is attributed to $ZrO_6$ and $HfO_6$ distortions. This peak intensifies in the LZOE and LHOE NPs compared to the LZO and LHO NPs. Such changes are ascribed to increasing distortion as a result of the fraction of $Eu^{3+}$ ion occupying $ZrO_6$ and $HfO_6$. The distortion resulted from lattice strain arises due to size and charge mismatch. Charge mismatch invokes the need for charge compensating defects which is oxygen vacancy when $Eu^{3+}$ ions occupy $Hf^{4+}$/$Zr^{4+}$ sites.

SEM images of the LZO and LHO NPs (Figure S4) show similar morphological characteristics: either spheroidal or spherical, highly uniform particles and certain degree of agglomeration. The average particle size of the LZO NPs is about 30–35 nm, obtained from the SEM images by averaging 50 particles, and it is smaller than the LHO NPs whose size is about 45–50 nm.

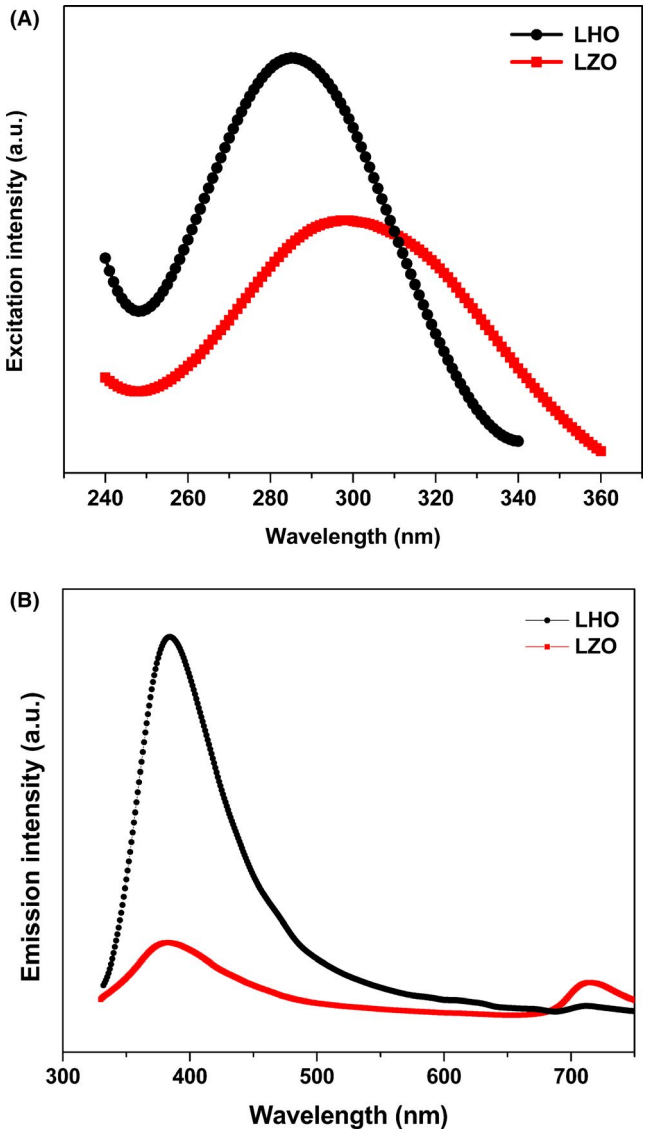


**FIGURE 2** PL (A) excitation ($\lambda_{em}$ = 400 nm) and (B) emission spectra ($\lambda_{ex}$ = 306 nm) of the LZO and LHO NPs [Color figure can be viewed at wileyonlinelibrary.com]

To verify the presence of Eu in the LHOE and LZOE NPs, they were analyzed by energy-dispersive X-ray spectroscopy (EDS). The estimated composition of the NPs is presented in Table S1.The EDS spectra (Figure S3) clearly revealed that the peaks correspond to O, Zr/Hf, La, and Eu from the LHOE and LZOE NPs.[39]

## 3.2 | Probing observed PL differences of LZO and LHO NPs by DFT calculations

Under emission wavelength of 400 nm, excitation spectra of the LZO and LHO NPs displayed a very broad and intense band at ~306 and 286 nm, respectively (Figure 2A), which are attributed to intrinsic electronic transition within the $ZrO_6$/$HfO_6$ polyhedra. The slight red shift of the excitation band from the LZO NPs compared to the LHO NPs

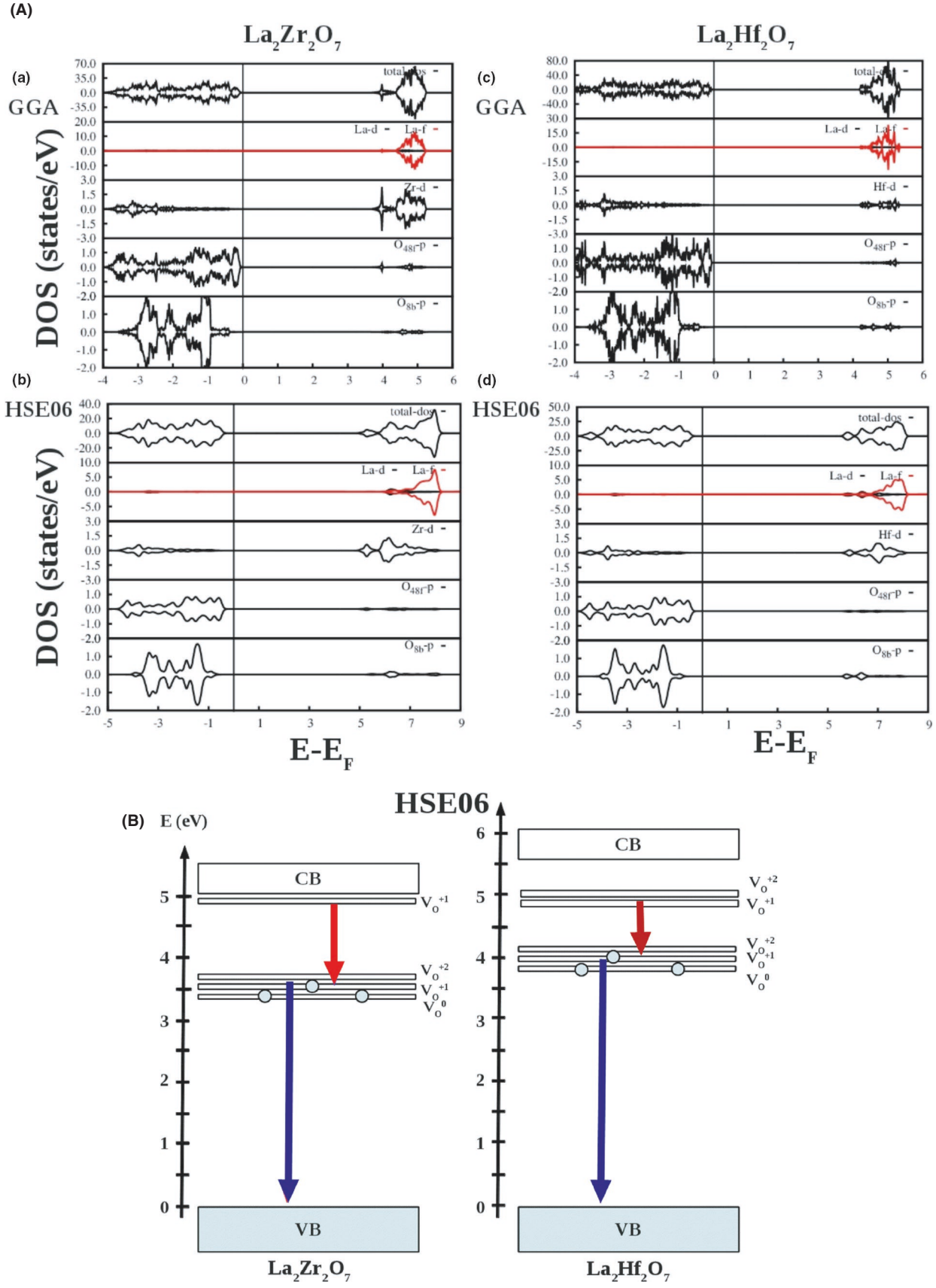


**FIGURE 3** (A) Comparison of (a) LZO GGA, (b) LZO HSE06, (c) LHO GGA and (d) LHO HSE06 calculated total and angular momentum decomposed density of states (DOS) in the ideal crystal structure. (B) Location of the defect states (calculated using DFT-HSE06) in the electronic bandgap of LZO and LHO in neutral ($V^{0}_{O}$) and charged defect sates ($V^{+1}_{O}$ and $V^{+2}_{O}$) [Color figure can be viewed at wileyonlinelibrary.com]

is attributed to the higher electronegativity of $Zr^{4+}$ ions compared to $Hf^{4+}$ ions, which makes the electronic transition in the case of $O^{2-} \rightarrow Zr^{4+}$ easier than that of $O^{2-} \rightarrow Hf^{4+}$. Emission spectrum of the LZO NPs under 306 nm excitation (Figure 2B) displayed a dual band feature at violet-blue and red regions around 400 and 700 nm, respectively. The emission around 400 nm (violet-blue) cannot be due to exciton emission due to large band gap of $La_2Zr_2O_7$. However, it is in close resemblance with the oxygen vacancies related emission in $ZrO_2$[47] and is attributed to the $^2T_{1u} \rightarrow {}^2A_{1g}$ transitions of $F^+$ center around the octahedral Zr atom. The red emission band around 707 nm band can be assigned to the transition of electron trapped at the shallow states to the vacant deep sates arising due to singly charged paramagnetic oxygen vacancy ($V_O{}^+$). On the other hand, the emission spectrum of the LHO NPs under 306 nm excitation displayed only one violet-blue emission with no signature of red band (Figure 2B).

In order to probe the reasons for the difference in the emission characteristics observed from the LZO and LHO NPs, we have calculated their electronic density of states (DOS) using density functional theory (DFT) based first-principles calculations. The DFT based calculations were performed on ideal LZO/LHO lattices and defective lattices in the presence of neutral ($V^0{}_O$) and charged ($V^{+1}{}_O$, $V^{+2}{}_O$) oxygen defects. Our DFT calculations show localization of defect states in the electronic band gap region of LZO and LHO. Figure 3A compares our DFT calculated electronic DOS of ideal LZO and LHO lattice using generalized gradient approximation (GGA) and hybrid functional (HSE06) for the exchange-correlation interaction. DOS calculation results of LZO/LHO with oxygen defects are provided in Figure S5. Figure 3A clearly shows very similar basic hybridization and electronic structures of ideal LZO and LHO lattices calculated using GGA and HSE06. Figure 3B illustrates a summary of defect states that arises in our DOS calculations with hybrid functional (HSE06) in the presence of $V^0{}_O$, $V^{+1}{}_O$. and $V^{+2}{}_O$ defects. Based on the location of the defect states in the electronic bandgaps of LZO and LHO in neutral and charged defect states (Figure 3B), defect states near 3.5 eV are consisted of $V_O{}^0$, $V_O{}^{+1}$, and $V_O{}^{+2}$ for LZO. Among them, the $V_O{}^0$ states are filled with electrons (shown by two circles) and the $V_O{}^{+1}$ state is partially filled (shown by one circle). The $V_O{}^{+2}$ states are vacant. The blue emission from both LZO and LHO NPs is explained as electronic transition from defect state localized around 3.5 eV to valence band. On the other hand, the red emission from the LZO NPs was attributed to electronic transition from defect state near CB to defect state located 1.5 eV below. In LHO, there is no such defect state near CB, but defect states are present almost 0.6 eV away from CB. Transition from those states to other defect states (which are present almost 1.0 eV below) gives emission in IR region.

Oxygen vacancies induced emission in blue and green regions have been observed previously from rare earth zirconate $Gd_2Zr_2O_7$ and $Nd_2Zr_2O_7$.[28,29] To confirm the origin of the emission bands from the LZO and LHO NPs, they were further annealed in oxidizing and reducing atmospheres.

To rule out the formation of any unwanted phase after annealing in an oxidizing pure oxygen (O), air, and a reducing (8% $H_2$ + 92% Ar, R) atmospheres, XRD data were taken for these annealed LZO and LHO NPs (Figure S6). The XRD patterns did not reveal the formation of any other phases, which indicates that they are stabilized as $La_2Zr_2O_7$ and $La_2Hf_2O_7$ pyrochlore NPs. Compared to that of the as-synthesized LZO and LHO NPs, the intensity of the emission bands decreases after annealed in oxygen (LZO-O and LHO-O) whereas it increases after annealed in reducing hydrogen (LZO-R and LHO-R) atmosphere (Figure 4). Oxygen molecules presented in the oxidizing atmosphere combine with the oxygen vacancies presented in the as-synthesized LZO and LHO NPs during the thermally annealing process, so the number of oxygen vacancies decrease and the emission intensity decreases. On the other hand, the increase in emission intensity after annealed in reducing Ar + $H_2$ atmosphere can be explained by the increase in oxygen vacancies, so the PL emission intensity increases.

### 3.3 | Corroborate the different optical properties of LZOE and LHOE NPs with DFT calculations

To understand the different optical properties of the LZOE and LHOE NPs, PL excitation, emission, lifetime and RL spectroscopic studies were carried out. The excitation spectra of the LZOE and LHOE NPs monitored at 612 nm, which corresponds to the $^5D_0 \rightarrow {}^7F_2$ transition of $Eu^{3+}$ ion, consist of a broadband in the range of 240–300 nm and several fine narrow peaks in the range of 350–500 nm attributed to intra f–f transitions of europium ion (Figure 5A).

The broad band is known as charge transfer band (CTB) and has combined contribution from various electronic transitions such as O → Eu, O → Hf/O → Zr and Hf → Eu/Zr → Eu although the dominant one should be the O → Eu transition.[48] The first difference of these two excitation spectra is the CTB position. The CTB of the LZOE NPs is blue shifted compared with that of the LHOE NPs. This phenomenon is attributed to higher electronegativity of Zr than Hf on the Pauling scale. This electronegativity difference makes the O → Eu electronic transition in the LZO host more difficult compared to that in the LHO host. Therefore, CTB of the LZOE NPs is at higher energy compared to that of the LHOE NPs.

The emission peaks at 361, 378, 393, 412, and 465 nm are attributed to intra f–f transitions of europium ion as $^7F_0 \rightarrow {}^5D_4$, $^7F_0 \rightarrow {}^5L_{7,8}$, $^7F_0 \rightarrow {}^5L_6$, $^7F_0 \rightarrow {}^5D_3$, and $^7F_0 \rightarrow {}^5D_2$,

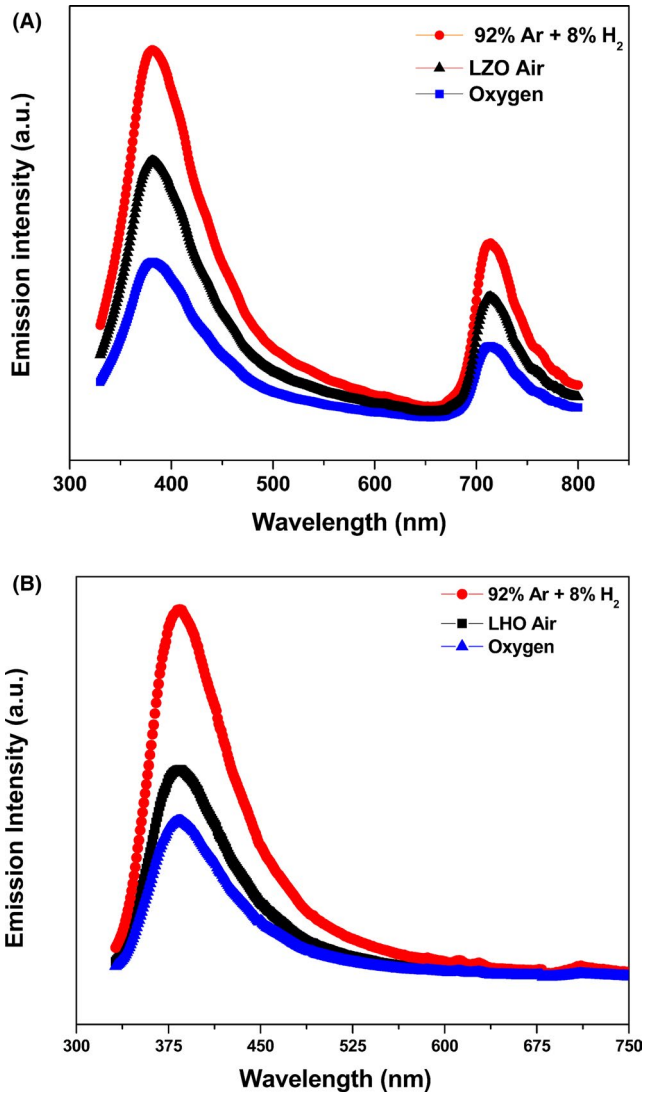


**FIGURE 4** Emission spectra of the (A) LZO and (B) LHO NPs before and after annealed in reducing (LZO-R and LHO-R) and oxidizing atmospheres (LZO-O and LHO-O) [Color figure can be viewed at wileyonlinelibrary.com]

respectively. Second, the relative intensity of the f–f band to the CTB of the LZOE NPs is weaker than that of the LZOE NPs. The f–f transitions are forbidden in nature whereas the CTB is allowed, which make the CTB transition probability higher than the former. All current commercial phosphors are excited by near UV or blue light. Excitation band arising from the $^7F_0 \rightarrow {}^5L_6$ (≈393 nm) and $^7F_0 \rightarrow {}^5D_2$ (≈465 nm) transitions are very attractive for color converter applications because they efficiently overlap with the emission spectra of near-UV (NUV) and blue light emitting diodes (LEDs), respectively. Therefore, the LHOE NPs are expected to have better performance over the LZOE NPs for lighting applications.

Emission spectra from the LZOE and LHOE NPs under CTB excitation (Figure 5B) exhibit similar profiles with typical emission bands of $Eu^{3+}$ transitions from the excited $^5D_0$ state to $^7F_J$ (J = 0, 1, 2, 3 and 4) ones. Specifically, the peaks located at 579, 592, 613, 654, and 710 nm are ascribed to the $^5D_0 \rightarrow {}^7F_0$, $^5D_0 \rightarrow {}^7F_1$, $^5D_0 \rightarrow {}^7F_2$, $^5D_0 \rightarrow {}^7F_3$, and $^5D_0 \rightarrow {}^7F_4$ transitions of europium ion, respectively. There are three characteristic differences from these two emission spectra: (a) the LHOE NPs have higher emission intensity under the same measurement conditions, (b) the asymmetric ratio ($I_{5D0\rightarrow7F2}/I_{5D0\rightarrow7F1}$) of the LHOE NPs (3.68) is higher than that of the LZOE NPs (3.29), and (c) the intensity of the two peaks located at 612 and 627 nm from the $^5D_0 \rightarrow {}^7F_2$ transition is the same for the LZOE NPs but is different for the LHOE NPs. Emission spectral features (b) and (c) indicate that the structural environment around europium ion is more asymmetric for the LHOE NPs compared to the LZOE NPs. Large asymmetric environment allows large oscillator strength for f–f transition and therefore more red emission intensity in case of LHOE compared to LZOE.

Luminescence decay profiles displayed bi-exponential decay with lifetime values of $\tau_1 = 0.836$ μs and $\tau_2 = 2.146$ ms ($\chi^2 = 1.142$) for the LZOE NPs (Figure 5C) and $\tau_1 = 1.260$ μs and $\tau_2 = 2.928$ ms ($\chi^2 = 1.127$) for the LHOE NPs (Figure 5D). This is attributed to stabilization of $Eu^{3+}$ ions at two types of sites: the highly asymmetric $La^{3+}$ sites (scalenohedra) and the symmetric $Hf^{4+}/Zr^{4+}$ sites (octahedra). $Eu^{3+}$ ions at both $La^{3+}$ and at $Zr^{4+}/Hf^{4+}$ sites decay at different rates although the fraction of $Eu^{3+}$ ions at $La^{3+}$ sites are more than that of $Eu^{3+}$ ions at $Zr^{4+}/Hf^{4+}$ sites due to the closeness in size and ionic charge. The longer lifetime is attributed to $Eu^{3+}$ ions at $Zr^{4+}/Hf^{4+}$ sites with more symmetric environment, which makes the f–f transition more forbidden. On the other hand, the shorter lifetime is attributed to $Eu^{3+}$ ions at $La^{3+}$ sites as f–f transition becomes more allowed in asymmetric environment and therefore decay in shorter time. Average lifetime and individual lifetimes of the LHOE NPs are longer than the LZOE NPs, which is attributed to the larger surface defect density of the LZOE NPs due to smaller particle size.

The emission spectra of the LZOE and LHOE NPs under excitation with CTB in extended region of 350–750 nm (Figure 6A) display typical features of $Eu^{3+}$ ions with $^5D_0 \rightarrow {}^7F_J$ ($J$ = 0–4) transitions with various electric and magnetic dipole transitions. Interestingly, the extent of host to $Eu^{3+}$ photon energy transfer (ET) is substantially higher from the LHOE NPs compared to the LZOE NPs evident from the presence of substantial violet-blue host emission due to oxygen vacancies. Moreover, the lifetimes of the LHO NPs ($\lambda_{ex}$ = 286 nm and $\lambda_{em}$ = 400 nm) and the LZO NPs ($\lambda_{ex}$ = 286 nm and $\lambda_{em}$ = 400 nm) are 9.6 and 6.1 μs, respectively. The energy transfer efficiency from the host to activator $Eu^{3+}$ ions can be calculated by $\eta_{ET} = 1 - \tau/\tau_0$ where $\tau$ and $\tau_0$ are the lifetimes of the host with and without the doping of $Eu^{3+}$. The lifetime of LHO host in the LHOE NPs is 3.9 μs whereas that of LZO host in the LZOE NPs is 4.6 μs. This leads to ET efficiency of 59.3% and 24.6% for the LHOE and LZOE NPs, respectively (Figure 6B). Because both LZOE

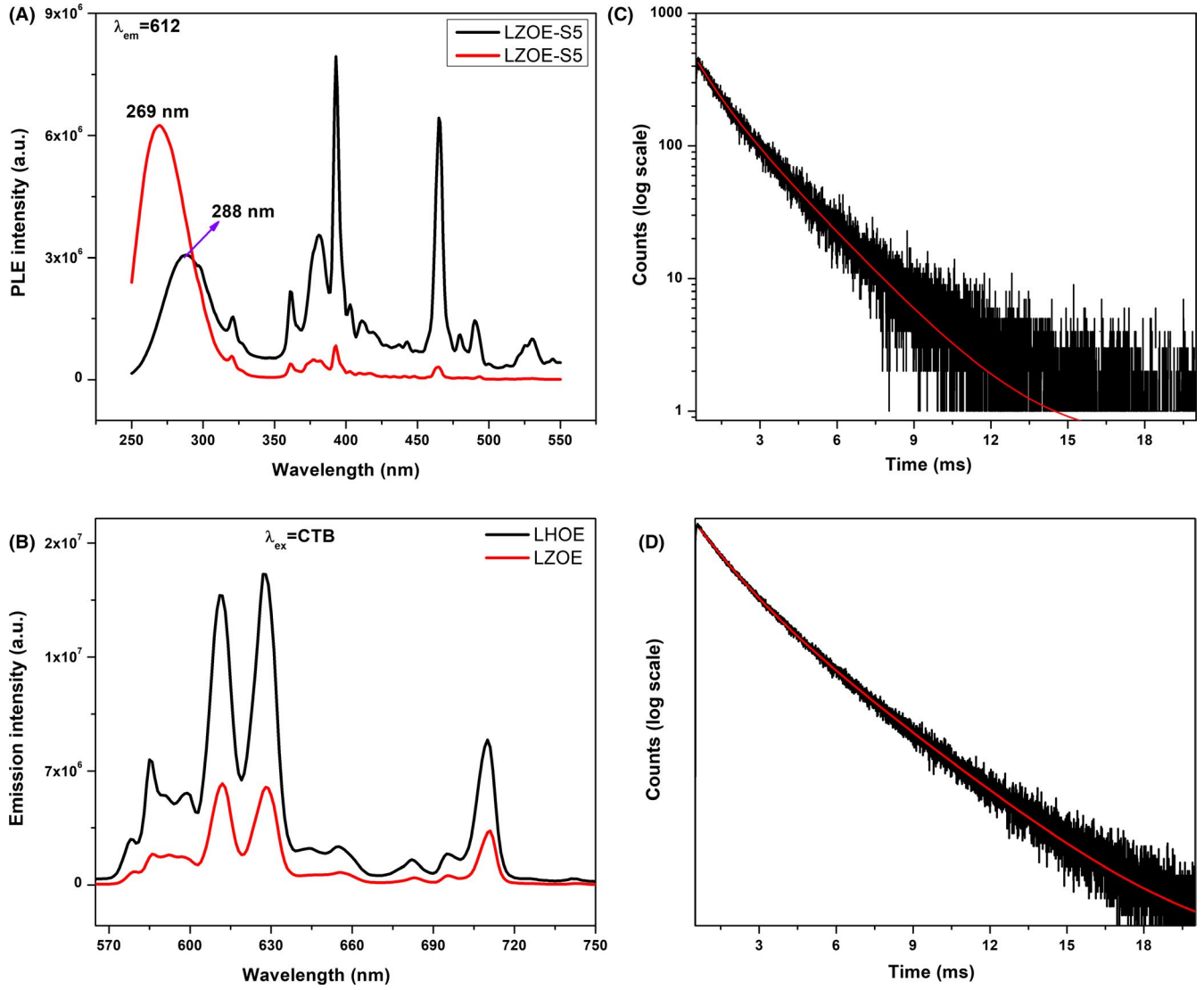


**FIGURE 5** Optical properties: PL (A) excitation and (B) emission spectra of the LZOE and LHOE NPs. PL decay profiles of the (C) LZOE and (D) LHOE NPs [Color figure can be viewed at wileyonlinelibrary.com]

and LHOE NPs are synthesized by the MSS method with 5.0% $Eu^{3+}$ doping under identical synthesis conditions, we have also performed DFT calculations as discussed in the subsequent section.

The RL spectra (Figure 7) of the LZOE and LHOE NPs are very similar to the PL spectra. The RL spectra also show the typical emission lines of $Eu^{3+}$ 4*f*–4*f* transitions in the red spectral region. No host-related emission in the violet-blue region was observed. This is because $Eu^{3+}$ ions are more effective trapping centers for electrons than oxygen defects. RL intensity from the LHOE NPs is higher than that from the LZOE NPs, which could be attributed to lower non-radiative channels, so lower surface defect density of the LHOE NPs with larger particle size than that of the LZOE NPs.

Table 2 highlights the various photophysical parameters for both the LZOE and LHOE NPs. The LHOE NPs have higher quantum efficiency (QE) than the LZOE NPs (both internal and absolute, IQE and AQE). This is correlated with the higher non-radiative transition rates ($A_{NR}$) of the LZOE NPs (251.9 $s^{-1}$) and the LHOE NPs (150.8 $s^{-1}$).

Non-radiative transition probability depends on several non-radiative decay pathways. One of the probable routes for the same is multiphonon relaxation (MPR) wherein several phonons needed for crossing energy difference between $^5D_0$ and $^7F_2$ levels ($\Delta J = \pm 2$, hypersensitive transition) of $Eu^{3+}$ ion. Phonon energy is one of the most important selection criteria for a luminescence host as it dictates the quanta of non-radiative pathways directly affecting the quantum efficiency of phosphors. The maximum optical phonon frequency ($\omega_{op}$) is inversely proportional to square root of mass of A and B atom according to equation:[49]

$$E_{ph} = \frac{h}{2\pi}\omega_{op}\sqrt{\frac{2g}{m_A + m_B}} \quad (1)$$

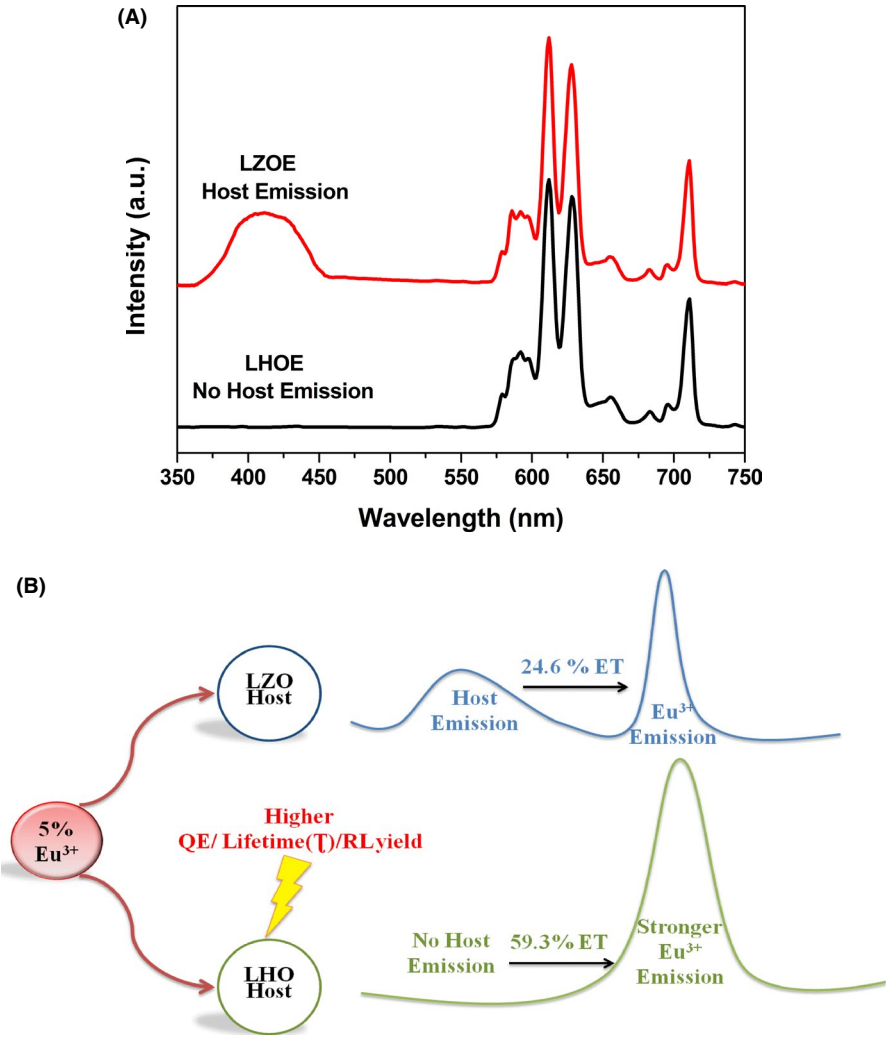


**FIGURE 6** (A) Emission spectra of the LHOE and LZOE NPs in the range of 350–750 nm under $\lambda_{ex}$ = CTB and (B) Schematic showing the effect of energy transfer on the optical performance of the LHOE and LZOE NPs [Color figure can be viewed at wileyonlinelibrary.com]

where $m_A$ and $m_B$ are the atomic mass of La and Zr/Hf, and $g$ is the interatomic potential. The fact that atomic mass of Hf (178.49) is much larger than that of Zr (91.22) reducing the optical phonon frequency of LHO compared to LZO. The low phonon energy of LHO (745 $cm^{-1}$) compared to LZO (785 $cm^{-1}$) is responsible for low $A_{NR}$ value and higher quantum efficiency of LHOE over LZOE.[49]

Higher Judd-Ofelt parameter $\Omega_2$ value of the LHOE NPs suggests that the environment around $Eu^{3+}$ ions in the LHO lattice is more polarizable and highly covalent compared with that in the LZO lattice. Due to the more polarizable nature of the Eu–O bond in the LHOE NPs, there is more distortion in electronic environment around the $Eu^{3+}$ ions at the $La^{3+}$ sites of the LHOE NPs compared with that of the LZOE NPs. Higher red emission from the LHOE NPs than that from the LZOE NPs is attributed to the more asymmetry environment around $Eu^{3+}$ ions in the LHO host, which relaxes the Laporte's forbidden f–f transitions, thereby increasing its oscillator strength.

To further understand the differences of the measured optical properties from the LZOE and LHOE NPs, DFT GGA was used to calculate DOS of LHO and LZO with $Eu^{3+}$ ions doping at $La^{3+}$ sites for no defect, +1 oxygen vacancy ($V_O^{+1}$) and + 2 oxygen vacancy ($V_O^{+2}$) situations for comparison (Figure 8). The distinctive features

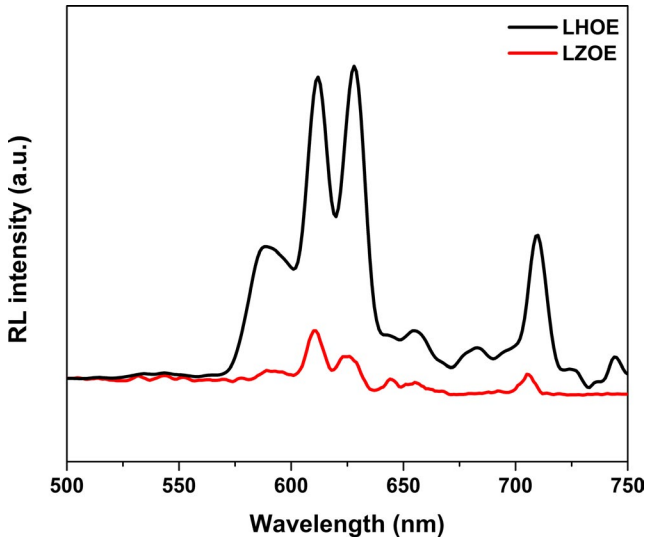


**FIGURE 7** Radioluminescence spectra of the LZOE and LHOE NPs [Color figure can be viewed at wileyonlinelibrary.com]

**TABLE 2** Various photophysical parameters of the LZOE and LHOE NPs

| Samples | $A_R$ ($s^{-1}$) | $A_{NR}$ ($s^{-1}$) | IQE (%) | $\Omega_2$ ($10^{-20}$ $cm^2$) | $\Omega_4$ ($10^{-20}$ $cm^2$) | $\beta_1$ | $\beta_2$ | $\beta_4$ | AQE (%) |
|---|---|---|---|---|---|---|---|---|---|
| LZOE | 272 | 252 | 54.1 | 1.98 | 1.51 | 18 % | 62 % | 17 % | 10.01 |
| LHOE | 269 | 150 | 74.9 | 2.05 | 1.06 | 19 % | 64 % | 15 % | 19.29 |

between $Eu^{3+}$ doped in LHO and LZO are as follow: (a) Eu *d*-states are bonded more strongly in LHO compared to LZO for the no defect situation due to the presence of higher amount of bonding and anti-bonding states in VB and CB, respectively, in LHO than that of LZO. Eu-*f* states are distributed almost throughout the VB of LHO, which is in contrast to LZO where *f*-states are only distributed over the top edge region of VB maxima. Eu-*f* states are present in both VB and CB regions in majority and minority spin components of LHO. On the contrary, Eu-f states are localized only over the top edge region of VB maxima in both majority and minority spin components of LZO, and no Eu-f state presents in its CB region. This means, less bonding between host and dopant atom in the LZOE NPs and hence less efficient energy transfer compared to that of the LHOE NPs. (b) Under the $V_O^{+1}$ and $V_O^{+2}$ situations, the number of impurity states created due to $Eu^{3+}$ doping is higher in LZOE compared to LHOE. In LZOE, the generated impurity states due to $Eu^{3+}$ doping are situated near to the oxygen defect states (in terms of energy range) and in other energy regions. On the contrary, in LHOE, $Eu^{3+}$ doping states are present at exact energy position (both in majority and minority spin components) where oxygen defect states are located. As a result, energy transfer process is more efficient in LHOE compared to LZOE, consistent with our experimental observations shown in Figures 5 and 7. This is in line with higher experimental energy transfer

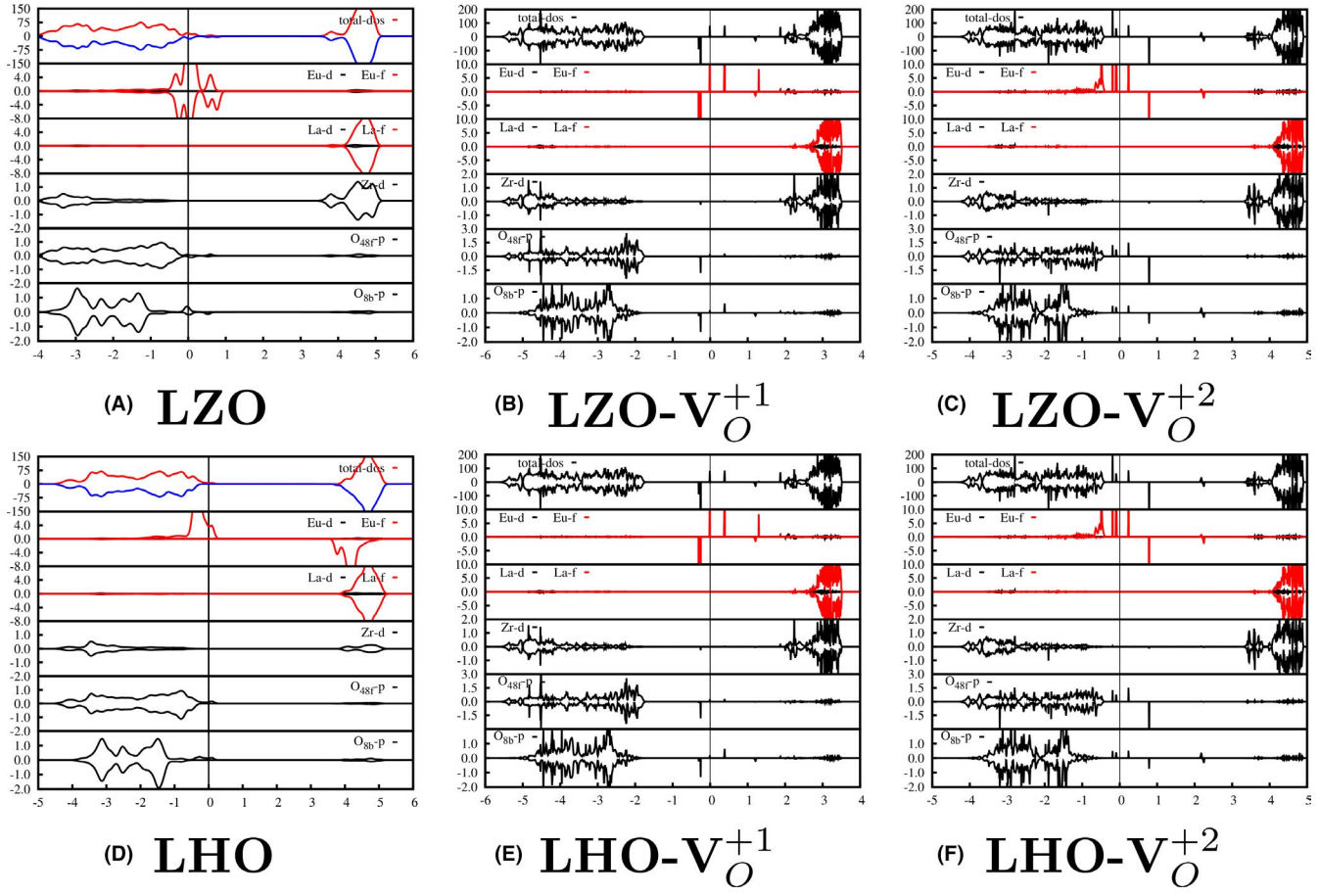


**FIGURE 8** A comparison of DFT-GGA calculated total and angular momentum decomposed DOS of LHO and LZO with Eu doping in (A)/(D) ideal LZO/LHO pyrochlore, (B)/(E) LZO/LHO with oxygen vacancy of +1 charge ($VO^{+1}$), and (C)/(F) LZO/LHO with oxygen vacancy of +2 charge ($VO^{+2}$), respectively. Vertical lines at 0 eV present Fermi energy. Eu doping was made in La site in all cases [Color figure can be viewed at wileyonlinelibrary.com]

efficiency from the LHOE NPs (59.3 %) compared with the LZOE NPs (24.6%).

### 3.4 | Luminescence photobleaching

The characterization of the luminescence photobleaching properties was performed for a small percentage of non-specifically surface-bound particles. It is essential not to excite particles in solution since the luminescence signal from floating particles results in uneven background. In total internal reflection fluorescence (TIRF) microscope, laser light is incident with the critical angle and reflected off at the interface between glass sample chamber (higher index of refraction) and buffer (lower index of refraction). However, it generates an evanescent field whose intensity decays exponentially so that luminescence particles within about 200 nanometers are excited while the ones above this region are not excited. Therefore, it allows us to characterize the luminescence photobleaching properties of only surface-bound particles.[50,51]

In fluorescence-based assays use of high-power excitation beam may lead to high background noise due to autofluorescence and non-specific interaction. Such intense power beam may also cause photobleaching in imaging and sample damage in in-vivo measurements. Regarding the reported exploration of organic molecules and quantam dots (QDs), the former including lanthanide chelates have issue of photobleaching whereas the latter have problems of low solubility and autofluorescence.[52] In this study, we also aim at more rigorous characterization of the possible photobleaching of the LZOE and LHOE NPs by measuring their luminescence intensities in real-time.[50,51] The sample preparation details for photobleaching experiment were mentioned in Figure S4.

Under our buffer condition, both the LHOE and LZOE NPs tended to form clusters (Figure 9). To rigorously investigate the luminescence photobleaching, the luminescence intensity of the nanoparticle samples marked by the yellow boxes (Figure 9) along those from nearby background space were analyzed. Both the LHOE and LZOE NPs did not show a noticeable degree of photobleaching during the 10 minutes observation time. Without a reduction in their light emitting efficiency, the LZOE and LHOE NPs allow continuous excitation and repetitive analysis. Such stability of exhibiting high luminescence efficiency without photobleaching from the LZOE and LHOE NPs enables high specific signals, and hence sensitive assays. This is attributed to the high luminescence of the LZOE and LHOE NPs happening within the host lattice.[53]

## 4 | DISCUSSION

In the surge to explore the performance of pyrochlore LZO and LHO NPs as photo- and radio-luminescence hosts, various experimental data based on time resolved PL and RL were

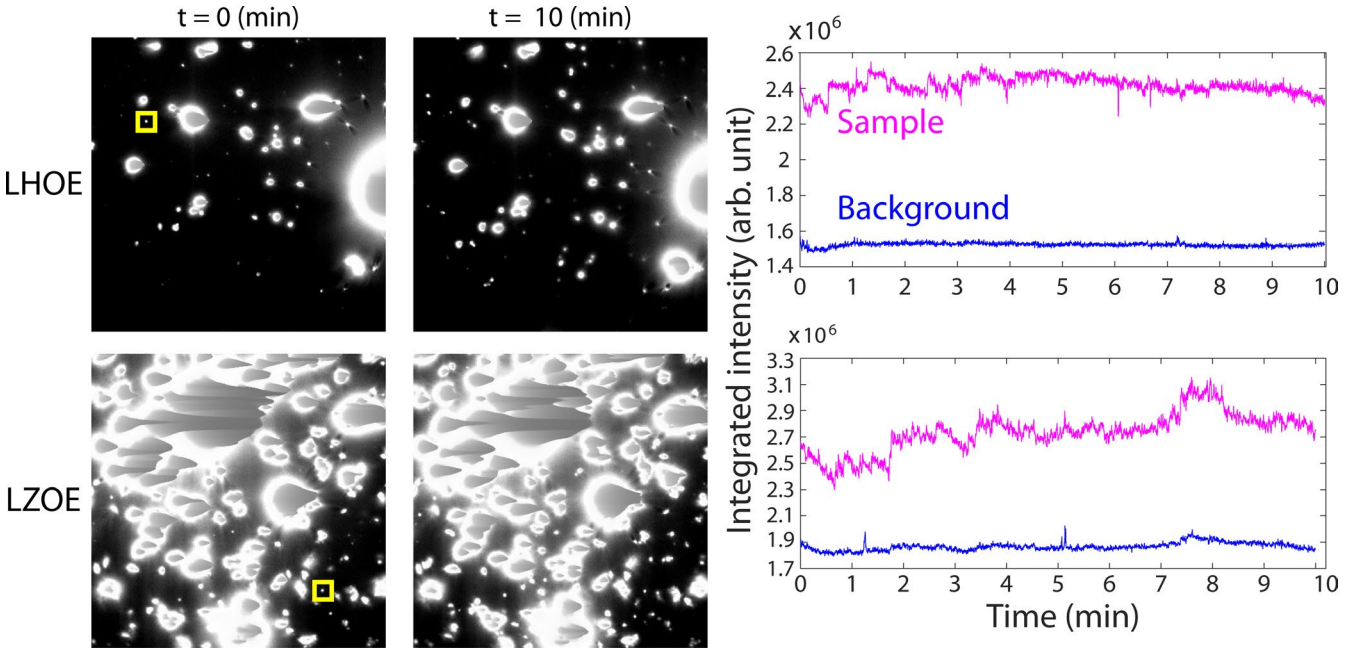


**FIGURE 9** Real-time measurements of luminescence upon 532 nm laser illumination using a total internal reflection fluorescence (TIRF) microscope. The figures in the first two columns represent snapshots at $t = 0$ and $t = 10$ minutes, respectively. Luminescence intensities of nonspecifically surface-bound NPs marked by the yellow squares in the first column were investigated as shown in the last column. The magenta and blue colored plots in the last column represent luminescence signal and background intensities, respectively. TIRF images: 81.9 × 81.9 μm [Color figure can be viewed at wileyonlinelibrary.com]

presented and the observed results were corroborated with our theoretical calculations. Based on PL studies, the differences in the optical properties of undoped LZO and LHO NPs are attributed to different defect states involved in their respective emission processes and are explained energetically in Figure 3B. The different positions of oxygen vacancies in their respective band gaps are responsible for emission spectra in different regions of the electromagnetic spectrum. Moreover, it was found the LHO NPs are better candidate host for $Eu^{3+}$ dopant under UV and X-ray excitations compared to the LZO NPs. This is attributed to better particle characteristics of the LHOE NPs in terms of crystallinity, surface defects and agglomeration than those of the LZOE NPs. DFT based calculations further suggested an efficient host to dopant energy transfer exists in LHOE compare to LZOE, which makes the luminescence process more efficient for the former and leads to enhanced emission output, quantum yield and excited state lifetime. In general, we have successfully probed the optical differences of the LZOE and LHOE NPs and found that the LHOE NPs are a better candidate for highly efficient luminescent devices and other applications such as red phosphors, fluoroimmunoassays, white LEDs and X-ray detectors. The designed NPs also exhibited high resistant to photobleaching which makes them good candidates for fluoroimmunoassay. However, further structural details of $Eu^{3+}$ ions in these LZOE and LHOE NPs should be explored using neutron diffraction and x-ray absorption spectroscopy to yield more insightful information in the near future.

## 5 | CONCLUSION

In this study, we have compared the optical properties of both undoped and $Eu^{3+}$-doped lanthanum zirconate and lanthanum hafnate nanoparticles by photoluminescence and radioluminescence spectroscopy. Emission spectroscopy with UV irradiation showed violet-blue emission from the LHO NPs and both violet-blue and red emissions from the LZO NPs. In addition, DFT calculations suggested different energetics of ionized oxygen vacancies in the LHO and LZO NPs, which are responsible for the observed emission differences. Luminescence spectroscopy of the $La_2Zr_2O_7:Eu^{3+}$ (LZOE) and $La_2Hf_2O_7:Eu^{3+}$ (LHOE) NPs showed higher quantum yield, emission output, radioluminescent intensity and luminescence lifetime. However, the LHOE NPs were superior in all aspects compared to the LZOE NPs. This information can be highly beneficial in the development of newer pyrochlore materials for red phosphors, scintillators and fluoroimmunoassays. The optimum performance of the LHOE NPs is attributed to its superior particle characteristics such as lower surface defects, lower optical phonon frequency and agglomeration etc. Based on DFT calculation, we proposed that the host to dopant energy transfer is more efficient for the LHOE NPs compared to the LZOE NPs, which is another factor responsible for the enhanced photoluminescence and radioluminescence efficiency of the LHOE NPs. Moreover, both the LZOE and LHOE NPs shows high photostability and can be highly beneficial in fluoroimmunoassays.

## ACKNOWLEDGMENTS

The authors thank the financial support by the National Science Foundation under CHE (award #1710160) and DMR (grant #1523577). SKG thanks the United States-India Education Foundation (USIEF) and the Institute of International Education (IIE) for the Fulbright Nehru Postdoctoral Fellowship (award #2268/FNPDR/2017). HK thanks the support from the UTRGV for start-up funding and the University of Texas System for the Rising Stars Award.

## ORCID

*Yuanbing Mao* https://orcid.org/0000-0003-2665-6676

## REFERENCES

1. Yang J, Han YI, Shahid M, Pan W, Zhao M, Wu W, et al. A promising material for thermal barrier coating: pyrochlore-related compound $Sm_2FeTaO_7$. Scripta Mater. 2018;149:49–52.
2. Jian S-K, Nie W. Weyl magnons in pyrochlore antiferromagnets with an all-in-all-out order. Physical Review B. 2018;97:115162.
3. Nguyen T, Sandilands LJ, Sohn C, Kim C, Wysocki AL, Yang I-S, et al. Two-magnon scattering in the 5 d all-in-all-out pyrochlore magnet $Cd_2O_2O_7$. Nat Commun. 2017;8:251.
4. Urban S, Djerdj I, Dolcet P, Chen L, Möller M, Khalid O, et al. In situ study of the oxygen-induced transformation of pyrochlore $Ce_2Zr_2O_{7+x}$ to the κ-$Ce_2Zr_2O_8$ phase. Chem Mater. 2017;29:9218–26.
5. Li N, Yin Y, Meng F, Zhang Q, Yan J, Jiang Q. Enabling pyrochlore-type oxides as highly efficient electrocatalysts for high-capacity and stable Na–$O_2$ batteries: the synergy of electronic structure and morphology. ACS Catal. 2017;7:7688–94.
6. Zhong F, Zhao J, Shi L, Xiao Y, Cai G, Zheng Y, et al. Alkaline-Earth metals-doped pyrochlore $Gd_2Zr_2O_7$ as oxygen conductors for improved $NO_2$ sensing performance. Sci Rep. 2017;7:4684.
7. Pokhrel M, Brik MG, Mao Y. Particle size and crystal phase dependent photoluminescence of $La_2Zr_2O_7:Eu^{3+}$ nanoparticles. J Am Ceram Soc. 2015;98:3192–201.
8. Shlyakhtina AV, Pygalskiy K, Belov D, Lyskov NV, Kharitonova E, Kolbanev I, et al. Proton and oxygen ion conductivity in the pyrochlore/fluorite family of $Ln_{2-x}Ca_xScMO_{7-\delta}$ (Ln= La, Sm, Ho, Yb; M= Nb, Ta; x= 0, 0.05, 0.1) niobates and tantalates. Dalton Trans. 2018;47:2376–92.
9. Perriot R, Dholabhai PP, Uberuaga BP. The role of surfaces, chemical interfaces, and disorder on plutonium incorporation in pyrochlores. Phys Chem Chem Phys. 2016;18:22852–63.
10. Pokhrel M, Wahid K, Mao Y. Systematic studies on $RE_2Hf_2O_7$: 5% $Eu^{3+}$ (RE= Y, La, Pr, Gd, Er, and Lu) nanoparticles: effects of the A-site $RE^{3+}$ cation and calcination on structure and photoluminescence. J Phys Chem C. 2016;27:14828–39.

11. Pokhrel M, Alcoutlabi M, Mao Y. Optical and X-ray induced luminescence from $Eu^{3+}$ doped $La_2Zr_2O_7$ nanoparticles. J Alloy Compd. 2017;693:719–29.
12. Wahid K, Pokhrel M, Mao Y. Structural, photoluminescence and radioluminescence properties of $Eu^{3+}$ doped $La_2Hf_2O_7$ nanoparticles. J Solid State Chem. 2017;245:89–97.
13. Zuniga JP, Gupta SK, Pokhrel M, Mao Y. Exploring the optical properties of $La_2Hf_2O_7$:$Pr^{3+}$ nanoparticles under UV and X-ray excitation for potential lighting and scintillating applications. New J Chem. 2018;42(12):9381–92.
14. Juyal A, Agarwal A, Mukhopadhyay S. Negative longitudinal magnetoresistance in the density wave phase of $Y_2Ir_2O_7$. Phys Rev Lett. 2018;120(9):096801.
15. Saitzek S, Shao Z, Bayart A, Ferri A, Huvé M, Roussel P, et al. Ferroelectricity in $La_2Zr_2O_7$ thin films with a frustrated pyrochlore-type structure. J Mater Chem C. 2014;2:4037–43.
16. Zhang F, Lang M, Liu Z, Ewing R. Pressure-induced disordering and anomalous lattice expansion in $La_2Zr_2O_7$ pyrochlore. Phys Rev Lett. 2010;105:015503.
17. Sangeetha NM, van Veggel FC. Lanthanum silicate and lanthanum zirconate nanoparticles co-doped with $Ho^{3+}$ and $Yb^{3+}$: matrix-dependent red and green upconversion emissions. J Phys Chem C. 2009;113:14702–7.
18. Chun J, Reuvekamp PG, Chen D, Lin C, Kremer RK. Promising high-k dielectric permittivity of pyrochlore-type crystals of $Nd_2Hf_2O_7$. J Mater Chem C. 2015;3:491–4.
19. Schroeder U, Richter C, Park MH, Schenk T, Pešić M, Hoffmann M, et al. Lanthanum-doped hafnium oxide: a robust ferroelectric material. Inorg Chem. 2018;57:2752–65.
20. Sevast'yanov VG, Simonenko EP, Simonenko NP, Sakharov KA, Kuznetsov NT. Synthesis of finely dispersed $La_2Zr_2O_7$, $La_2Hf_2O_7$, $Gd_2Zr_2O_7$ and $Gd_2Hf_2O_7$ oxides. Mendeleev Commun. 2013;23:17–8.
21. Srivastava A, Beers W. On the impurity trapped exciton luminescence in $La_2Zr_2O_7$:$Bi^{3+}$. J Lumin. 1999;81:293–300.
22. Pokhrel M, Burger A, Groza M, Mao Y. Enhance the photoluminescence and radioluminescence of $La_2Zr_2O_7$: $Eu^{3+}$ core nanoparticles by coating with a thin $Y_2O_3$ shell. Opt Mater. 2017;68:35–41.
23. Pokhrel M, Brik MG, Mao Y. Particle size and crystal phase dependent photoluminescence of $La_2Zr_2O_7$: $Eu^{3+}$ nanoparticles. J Am Ceram Soc. 2015;98:3192–201.
24. Liu R, Dong X, Wang J, Yu W, Liu G. Preparation, characterization and luminescence properties of pyrochlore $La_2Zr_2O_7$: $Eu^{3+}$ nanofibers by electrospinning. J Optoelectron Adv Mater. 2014;16:542–6.
25. Alaparthi SB, Tian Y, Mao Y. Synthesis and photoluminescence properties of $La_2Zr_2O_7$:$Eu^{3+}$@$YBO_3$ core@ shell nanoparticles. Nanotechnology. 2013;25:025703.
26. Vassen R, Cao X, Tietz F, Basu D, Stöver D. Zirconates as new materials for thermal barrier coatings. J Am Ceram Soc. 2000;83:2023–8.
27. Hansel RA, Desai S, Allison SW, Heyes A, Walker DG. Emission lifetimes of europium-doped pyrochlores for phosphor thermometry. AIP. 2010; 107:016101.
28. Gupta SK, Ghosh P, Reghukumar C, Pathak N, Kadam R. Experimental and theoretical approach to account for green luminescence from $Gd_2Zr_2O_7$ pyrochlore: exploring the site occupancy and origin of host-dopant energy transfer in $Gd_2Zr_2O_7$:$Eu^{3+}$. RSC Adv. 2016;6:44908–20.
29. Gupta SK, Sudarshan K, Ghosh P, Srivastava A, Bevara S, Pujari P, et al. Role of various defects in the photoluminescence characteristics of nanocrystalline $Nd_2Zr_2O_7$: an investigation through spectroscopic and DFT calculations. J Mater Chem C. 2016;4:4988–5000.
30. Zhang A, Lü M, Yang Z, Zhou G, Zhou Y. Systematic research on $RE_2Zr_2O_7$ (RE= La, Nd, Eu and Y) nanocrystals: preparation, structure and photoluminescence characterization. Solid State Sci. 2008;10:74–81.
31. Eagleman Y, Weber M, Chaudhry A, Derenzo S. Luminescence study of cerium-doped $La_2Hf_2O_7$: effects due to trivalent and tetravalent cerium and oxygen vacancies. J Lumin. 2012;132:2889–96.
32. Gupta SK, Ghosh P, Pathak N, Arya A, Natarajan V. Understanding the local environment of $Sm^{3+}$ in doped $SrZrO_3$ and energy transfer mechanism using time-resolved luminescence: a combined theoretical and experimental approach. RSC Adv. 2014;4:29202–15.
33. Pathak N, Ghosh PS, Gupta SK, Mukherjee S, Kadam RM, Arya A. An insight into the various defects-induced emission in $MgAl_2O_4$ and their tunability with phase behavior: combined experimental and theoretical approach. J Phys Chem C. 2016;120:4016–31.
34. Wang D-Y, Huang C-H, Cheng B-M, Chen T-M, Wang Y-H. Charge transfer luminescence of hafnates under synchrotron vacuum ultraviolet excitation. RSC Adv. 2014;54:28632–5.
35. Gupta SK, Bhide MK, Godbole SV, Natarajan V. Probing site symmetry around $Eu^{3+}$ in nanocrystalline $ThO_2$ using time resolved emission spectroscopy. J Am Ceram Soc. 2014;97:3694–701.
36. Gupta SK, Zuniga JP, Abdou M, Mao Y. Thermal annealing effects on $La_2Hf_2O_7$:$Eu^{3+}$ nanoparticles: a curious case study of structural evolution and site-specific photo- and radio-luminescence. Inorg Chem Front. 2018;5:2508–21.
37. Mani R, Gupta SK, Ghosh PS, Yellow JH. Emission from low coordination site of $Sr_2SiO_4$:$Eu^{2+}$, $Ce^{3+}$: influence of lanthanide dopants on the electron density and crystallinity in crystal site engineering approach. Chem A Eur J. 2018;24(60):16149–59.
38. Zuniga JP, Gupta SK, Abdou M, Mao Y. Effect of molten salt synthesis processing duration on the photo- and radioluminescence of UV-, visible-, and X-ray-excitable $La_2Hf_2O_7$:$Eu^{3+}$ nanoparticles. ACS Omega. 2018;3:7757–70.
39. Gupta SK, Abdou M, Zuniga JP, Ghosh PS, Molina E, Xu B, et al. Roles of oxygen vacancies and pH induced size changes on photo- and radioluminescence of undoped and $Eu^{3+}$-doped $La_2Zr_2O_7$ nanoparticles. J Lumin. 2019;209:302–15.
40. Zuniga JP, Abdou M, Gupta SK, Mao Y. Molten-salt synthesis of complex metal oxide nanoparticles. J Vis Exp. 2018;140:e58482.
41. Rabuffetti FA, Culver SP, Lee JS, Brutchey RL. Local structural investigation of $Eu^{3+}$-doped $BaTiO_3$ nanocrystals. Nanoscale. 2014;6:2909–14.
42. Savytskii D, Knorr B, Dierolf V, Jain H. Demonstration of single crystal growth via solid-solid transformation of a glass. Sci Rep. 2016;6:23324.
43. Kivambe M, Aissa B, Tabet N. Emerging technologies in crystal growth of photovoltaic silicon: progress and challenges. Energy Procedia. 2017;130:7–13.
44. Zhang C, Lin J. Defect-related luminescent materials: synthesis, emission properties and applications. Chem Soc Rev. 2012;41(23):7938–61.
45. Xu T, Wang G, Liang C, Pan M. N-doped $La_2Zr_2O_7$ as an enhanced electrocatalyst for oxygen reduction reaction. Electrochim Acta. 2014;143:83–8.

46. Gu S, Zhang S, Xue B, Yan J, Li W, Zhang L. Phase variation and thermophysical properties of $La_2Hf_2O_7$ with alumina addition. J Eur Ceram Soc. 2017;38(4):1938–45.
47. Liang J, Deng Z, Jiang X, Li F, Li Y. Photoluminescence of tetragonal $ZrO_2$ nanoparticles synthesized by microwave irradiation. Inorg Chem. 2002;41:3602–4.
48. Gupta SK, Ghosh PS, Sudarshan K, Gupta R, Pujari PK, Kadam RM. Multifunctional pure and $Eu^{3+}$ doped β-$Ag_2MoO_4$: photoluminescence, energy transfer dynamics and defect induced properties. Dalton Trans. 2015;44:19097–110.
49. Hansel RA, Desai SK, Allison SW, Heyes AL, Walker DG. Emission lifetimes of europium-doped pyrochlores for phosphor thermometry. J Appl Phys. 2010;107:016101.
50. Kim H, Selvin PR. Fluorescence imaging with one nanometer accuracy. In Roberts GCK, editor. Encyclopedia of Biophysics. Berlin, Heidelberg: Springer; 2013. https://doi.org/10.1007/978-3-642-16712-6_511
51. Yildiz A, Forkey JN, McKinney SA, Ha T, Goldman YE, Selvin PR. Myosin V walks hand-over-hand: single fluorophore imaging with 1.5-nm localization. Science. 2003;300:2061–5.
52. Ukonaho T, Rantanen T, Jämsen L, Kuningas K, Päkkilä H, Lövgren T, et al. Comparison of infrared-excited up-converting phosphors and europium nanoparticles as labels in a two-site immunoassay. Anal Chim Acta. 2007;596:106–15.
53. Beverloo HB, van Schadewijk A, Zijlmans HJ, Tanke HJ. Immunochemical detection of proteins and nucleic acids on filters using small luminescent inorganic crystals as markers. Anal Biochem. 1992;203:326–34.

## SUPPORTING INFORMATION

Additional supporting information may be found online in the Supporting Information section at the end of the article.

**How to cite this article:** Gupta SK, Abdou M, Ghosh PS, et al. On comparison of luminescence properties of $La_2Zr_2O_7$ and $La_2Hf_2O_7$ nanoparticles. *J Am Ceram Soc*. 2020;103:235–248. https://doi.org/10.1111/jace.16693